Received April 12, 2022, accepted May 4, 2022, date of publication May 9, 2022, date of current version May 12, 2022.

Digital Object Identifier 10.1109/ACCESS.2022.3173290

Linear Lag Models and Measurements of the Lag Correction Factors

EUNAE LEE, (Member, IEEE), AND DONG SIK KIM, (Senior Member, IEEE)
Department of Electronics Engineering, Hankuk University of Foreign Studies, Yongin 17035, South Korea

Corresponding author: Dong Sik Kim (dskim@hufs.ac.kr)

This work was supported in part by the National Research Foundation of Korea (NRF) grants funded by the Korean Government (MISP) under Grant 2020R1A2C1009895, and in part by the Hankuk University of Foreign Studies Research Fund of 2022.

ABSTRACT For fluoroscopic imaging, flat-panel dynamic detectors can acquire X-ray image sequences with frame rates higher than 300 frames per second. However, the sequentially acquired images have artifacts due to the lag signals, which are caused from trapping charges in the amorphous structure and incomplete reads. Furthermore, the lag signal lowers the noise power spectrum (NPS) of the detector; hence, the detector performance can be inflated. Conventional approaches for correcting the measured NPS are based on the lag correction factor (LCF). Various LCF measurement methods have been developed based on moving average and auto-regressive models. Current methods require high computational complexities with many images. In this paper, we first review the current methods and next propose three LCF measurement methods in simplified forms under an autoregressive model of order 1 based on the temporal periodogram mean and line means. Here, we suggest schemes that deal with several disturbances, such as nonuniform temporal gains and exposure leaks, to accurately measure LCF. A comparative review of the LCF measurement methods can establish a taxonomy of measurements. Through extensive experiments using X-ray images acquired from dynamic detectors, it is shown that the proposed methods yield comparable performances with lower computational complexities compared to the existing methods.

INDEX TERMS Auto-regressive model, flat-panel dynamic detector, lag correction factor, lag signal, moving average model, periodogram, power spectral density, X-ray image.

NOMENCLATURE

a	Parameter in AR(1).
D, R	Line mean difference and ratio.
$f_{MA,n}, f_{AR,n}$	Signals with lag for MA(L) and AR(1).
$\bar{f}_{MA,n}, \bar{f}_{AR,n}$	Decaying signals with lag and leak.
$\hat{f}_{MA,n}, \hat{f}_{AR,n}$	Decaying signals for pulse x-rays.
g_n, $\bar{g}_n$	Independent and decaying signals.
h_ℓ	Causal system for MA(L).
I_f, J_f	Spatial and temporal periodogram mean.
L	Order of the MA model.
N	Number of image frames.
NPS_f	Noise power spectrum of f.
q_n	Signal with nonuniform temporal gain.
r_{AR}	Lag correction factor for AR(1).
r_{MA}	Lag correction factor for MA(L).
U^2	Number of pixels per image.
u^o	Position of the x-ray off at $n = 0$.
α, ν	Frame gap and the signal per pixel period.
Δq	Image difference for the U-L scheme.
γ_n	Nonuniform temporal gain.
μ, μ_ϵ	Means of g and the exposure leak.
ρ_ℓ	Pearson correlation coefficient of $f_{MA,n}$.
ϕ_ℓ	Unit step function.

The associate editor coordinating the review of this manuscript and approving it for publication was Li Zhang.

I. INTRODUCTION

For fluoroscopic imaging, dynamic detectors can acquire X-ray image sequences with frame rates higher than 300 frames per second (fps). In flat-panel (FP) dynamic detectors [1] with amorphous Si or amorphous In-Ga-Zn-O (a-IGZO) thin-film transistor (TFT) panels [2], [3], trapping charges in the amorphous structure and incomplete reads yield lag signals to the subsequent exposed image frames [4]–[6]. Afterglows at the scintillator layer can also cause lag signals, which is usually much less than the case of trapping charges [7]. Because the main cause of the lag signals is incomplete reads, we can observe near constant lag signal magnitudes even when the frame interval is as small as 3ms. Sequentially acquired image frames have lag

artifacts, which appear in the form of temporal blurring and ghosting [8], [9]. The lag signals also affect diagnostic computed tomography (CT) and cone-beam CT reconstruction [10]–[12] in producing various lag artifacts. Hence, research has been conducted to solve various problems related to the lag signals [13], [14].

Noise properties of radiography detectors from photon and electric noise can be evaluated by measuring the noise power spectrum (NPS) [15]–[17], which is the power spectral density (PSD) of X-ray images acquired under specified irradiation conditions with uniform intensity [18]–[22]. However, the lag signal lowers the NPS curve; hence, the detector performance can be inflated. A correction technique for the measured NPS should be developed to determine the true detector noise performance. Conventional approaches for correcting the measured NPS are based on using the lag correction factor (LCF) [16], [23]–[27]. Designing detectors, which produce weak lag signals, is also important to reducing the lag artifacts. Accurately measuring the degree of lag signal strength can be a guideline for improving the lag performance [26], [27] by observing the effect of changes in incident doses, frame rates, readout circuits, TFT panels, and other possible factors. The LCF value has the maximal value of 1 if there are no lag signals. By measuring the LCF for a given dynamic detector, we can also evaluate the degree of lag signal strength.

In the literature, several LCF measurement methods have been proposed based on two types of linear lag models: the moving average and autoregressive models. The current methods can use the first moments, such as the mean, or the second moments, such as the variance, including the correlation and temporal PSD from acquired X-ray image frames [28, p. 296]. Here, the first and second moments can be obtained from transient decaying after the X-ray turns off and steady-state frames, respectively. The image frames can be obtained from a continuous X-ray with a constant potential generator [29, p. 301], [30, p. 14] through a continuous fluoroscopy mode or from a pulsed X-ray with switching through a pulsed fluoroscopy mode [29, p. 307] to reduce motion blurring [31, p. 322].

Matsunaga *et al.* [23] considered an autoregressive model of order 1 (AR(1)) [22, p. 787], [32, p. 886] to describe the lag signals in imaging systems. Subsequently, they proposed two measurement methods; the first one uses a correlation between two consecutive images, and the second one uses a mean ratio of fully exposed to the next non-exposed image. This ratio is commonly used to specify a lag performance for dynamic detectors in percent. Based on a moving average model of order L (MA(L)) [22, p. 788], [32, p. 886] several methods have been proposed as follows. Busse *et al.* [16], [25] considered a temporal periodogram mean to calculate the LCF based on the temporal PSD. This method is recommended in the IEC62220-1-3 standard [16]. However, in calculating PSD, various disturbances can distort the measured values. For example, in acquiring image frames under an X-ray source, the gains of image frames can be non-uniform because of inconsistent detector readout circuits as well as X-ray source. Hence, this nonuniform temporal gain (NTG) should be corrected to accurately estimate LCF, particularly when using PSD [25], [26], [33]. Furthermore, the PSD method has the disadvantage of using a lot of images (64 -128 images). Granfors and Aufrichtig [24] proposed a measurement method that uses the block means of frames acquired under the pulsed X-ray source. However, the IEC62220-1-3 standard recommends using a continuous X-ray source to control the X-ray quality [16]. Kim and Lee [26] proposed an extended method from the correlation-based method of Matsunaga *et al.* to a scenario of the MA(L) model, where a series of correlations are employed. To extend the Granfors-Aufrichtig method to the continuous X-ray source, Kim and Lee [27] proposed several methods based on line means.

In this paper, we first analyze and compare the existing LCF measurement methods based on the MA(L) and AR(1) models. Through the analyses and comparisons, we can predict various characteristics of the LCF values measured using existing methods. We next propose three LCF measurement methods in simplified forms based on the AR(1) model from the notions of the temporal periodogram mean [25] and line means [27]. The proposed methods can simply measure the LCF values by obtaining a single parameter from several images for the AR(1) model with performances comparable to those of the MA(L) model. To alleviate the NTG problem for the approach of PSD as well as correlations, we use a correction scheme called the upper-lower (U-L) scheme based on a notion of image difference [17], [26], [34]. A gate line scan of the TFT array is performed for an FP X-ray detector to read out charges from photodiodes of pixels [35], [36]. Leak currents can be generated and accumulated even when the TFT gates are off due to various conditions, such as incident light photons entering the TFT gates [35], [37], [38]. The leak current can produce crosstalk artifacts [35], [39] in radiography imaging and distort the measured LCF for the methods that are based on the line means [27]. For such methods, a technique for the exposure leak compensation is also considered in this paper.

The remainder of this paper is organized as follows. In Section II, we formulate the NPS and define two different LCF formulations. In Section III, we review the existing LCF measurement methods based on the MA(L) and AR(1) models. Subsequently, we propose three simple methods based on the AR(1) model in Section IV. Experimental results for dynamic detectors and discussions are presented in Section V, and the paper is concluded in the last section.

II. NOISE POWER SPECTRUM AND LAG CORRECTION FACTORS

In this section, we first formulate the NPS of a detector and next derive two formulations of LCF for the MA(L) and AR(1) models, respectively.

The NPS of noise can provide amounts of photon, electric, and fixed pattern noises of a dynamic detector [16]. The NPS

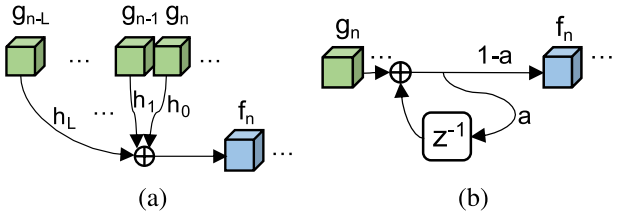

FIGURE 1. Linear lag models in fluoroscopic imaging. (a) Moving average model of order *L* (MA(*L*)). (b) Autoregressive model of order 1 (AR(1)).

values of a detector can be measured using the Fourier transform of the auto-covariance function of an image signal [19]. For practical measures of NPS [20], [21], [32], we generally use an empirical mean of periodograms [21, p. 112], [40], [41], where the mean is an asymptotically unbiased estimate of NPS [21].

For a sequence of uniformly exposed images, we consider a weakly stationary sequence $f_n[\boldsymbol{u}]$ with the mean of $\mu := E\{f_n\}$ and variance of $\mathrm{Var}\{f_n\}$, for the pixel position $\boldsymbol{u}$ of the nth image frame, where $\boldsymbol{u} := (u_1, u_2) \in \{0, \cdots, U-1\}^2$. Let I_f denote the periodogram mean of f_n defined as

$$I_f[\boldsymbol{v}] := E\left\{\frac{1}{U^2}\left|\sum_{\boldsymbol{u}}(f_n[\boldsymbol{u}]-\mu)\,\mathcal{W}_U^{\boldsymbol{u}^{\mathsf{T}}\boldsymbol{v}}\right|^2\right\}, \tag{1}$$

for $\boldsymbol{v} \in \{0, \cdots, U-1\}^2$, where u^{T} implies the transpose of vector u and $\mathcal{W}_U := e^{-2\pi j/U}$ [42, p. 235]. Let NPS_f denote the NPS of f_n for the nth frame. We then obtain an asymptotic relationship: $I_f \to NPS_f$, as $U \to \infty$ [21]. For practical measurements using the acquired f_n, we can obtain I_f from a smoothed periodogram of a sample mean of the periodograms based on the Bartlett-Welch method [40], [41].

Because the lag signal in FP dynamic detectors acts as a low-pass filter for the noise signals, measured NPS values are lower than those of a detector that has no lag signals [23]. The detective quantum efficiency (DQE) values are inversely proportional to the NPS values [16], [43, p. 311]. Hence, if we use these lower NPS values, the DQE values can be increased; in other words, the performance of a dynamic detector can be inflated incorrectly. To evaluate the detector performance correctly, we should correct the measured NPS values considering the effect of the lag signal. Relationships between the true and measured NPS values can be asymptotically obtained by calculating the periodogram means. Here, LCF can successfully describe the relationships [24].

From the literature on the lag signals, we can summarize two linear lag models: moving average and autoregressive models. In this section, we define two different LCF formulations depending on the lag models. The first lag model has a form of the MA(L) model [22, p. 288], [24], [32] as shown in Fig 1(a). For a pixel position $\boldsymbol{u}$, let $g_n[\boldsymbol{u}]$ denote a signal that is independent and identically distributed. The MA(L) model with a signal $f_{MA,n}$ is defined as

$$f_{MA,n}[\boldsymbol{u}] = \sum_{l=0}^{L} g_{n-\ell}[\boldsymbol{u}]h_\ell, \tag{2}$$

where h_ℓ is a causal system, such that $\sum_{\ell=0}^{L} h_\ell = 1$ with nonnegative h_ℓ [44]. Here, L is the order in the MA(L) model. Let $I_{f_{MA}}[\boldsymbol{v}]$ and $I_g[\boldsymbol{v}]$ denote the periodogram means of $f_{MA,n}$ and g_n, respectively, and are defined in (1). The periodogram means of the model in (2) satisfies $I_{f_{MA}}[\boldsymbol{v}] = r_{MA} I_g[\boldsymbol{v}]$, where r_{MA} implies the LCF under the MA(L) model and is defined as

$$r_{MA} := \sum_{\ell=0}^{L} h_\ell^2. \tag{3}$$

The LCF of (3) satisfies $0 < r_{MA} \le 1$ and thus $I_{f_{MA}}[\boldsymbol{v}] \le I_g[\boldsymbol{v}]$ holds. By using this LCF, we can asymptotically correct the measured NPS to obtain the true NPS from $NPS_g[\boldsymbol{v}] \approx NPS_{f_{MA}}[\boldsymbol{v}]/r_{MA}$.

The second linear lag model has a form of the AR(1) model [22, p. 287], [32] as shown in Fig.1(b) which is considered by Matsunaga *et al.* [23]. The AR(1) model with a signal $f_{AR,n}$ is then defined as

$$f_{AR,n}[\boldsymbol{u}] = a f_{AR,n-1}[\boldsymbol{u}] + (1-a) g_n[\boldsymbol{u}], \tag{4}$$

where the parameter a satisfies $0 \le a < 1$. From the AR(1) model in (4), we can obtain a relationship of $I_{f_{AR}}[\boldsymbol{v}] = r_{AR} I_g[\boldsymbol{v}]$, where r_{AR} implies the LCF under the AR(1) model and is defined as

$$r_{AR} := \frac{1-a}{1+a}. \tag{5}$$

Hence, the AR(1) model can simplify the measurement of LCF using only one parameter a. The LCF in (5) also satisfies $0 < r_{AR} \le 1$, and thus $I_{f_{AR}}[\boldsymbol{v}] \le I_g[\boldsymbol{v}]$ is similar to the MA(L) scenario. By using this LCF, we can also asymptotically correct the measured NPS to obtain the true NPS from $NPS_g[\boldsymbol{v}] \approx NPS_{AR,f}[\boldsymbol{v}]/r_{AR}$.

We now observe a relationship between the LCF values of r_{MA} and r_{AR}. When $h_\ell = (1-a)a^\ell$ in the LCF of (3), Kim and Lee [26] derived a relationship as

$$\lim_{L\to\infty} r_{MA}\big|_{h_\ell=(1-a)a^\ell} = r_{AR}. \tag{6}$$

For relatively small values of a, $(1-a)/(1+a) \approx (1-a)^2$ holds. In other words, we can obtain an approximation of $r_{MA} \approx r_{AR}$ for $L = 0$. Hence, the first coefficient $h_0 = (1-a)$ can be sufficient to calculate LCF, as Granfors and Aufrichtig discussed [24].

III. LAG CORRECTION FACTOR MEASUREMENTS

Various measurement methods for LCF have been proposed depending on the linear lag models and X-ray source types as summarized in Table 1. We review the existing methods in this section. We next introduce the AR1, AR3, and AR4 methods, which are listed in Table 1 as "Proposed" in the following section.

In Table 1, MA1−MA5 are methods of measuring LCF based on the MA(L) model and AR1−AR5 are based on the AR(1) model. MA1, MA2, AR1, and AR2 use the steady-state second moments [28, p. 296] of image frames acquired from both continuous and pulsed X-ray sources.

TABLE 1. Measurement methods for the lag correction factor (LCF) .

Input X-ray source	Steady-state second moments Continuous, pulsed		Transient first moments Continuous		Pulsed
MA(L) model	MA1 Busse *et al.* [25] IEC62220 [16]	MA2 Kim, Lee [26]	MA3 MA4 Kim, Lee [27]		MA5 Granfors, Aufrichtig [24]
AR(1) model	**AR1** **Proposed**	AR2 Matsunaga *et al.* [23]	**AR3** **AR4** **Proposed**		AR5 Matsunaga *et al.* [23]
Description	Temporal periodogram	Temporal correlation	Line mean Difference	Ratio	Block mean

Here, signal variances or periodograms are used. The method using steady-state image frames has the advantage that the X-ray does not need to be stopped halfway. As the first moment [28, p. 296] methods, where signal means are used, MA3, MA4, AR3, and AR4 use the transient decaying image frames acquired from the continuous X-ray source and MA5 and AR5 use the transient decaying image frames acquired from the pulsed X-ray source.

A. MA1: TEMPORAL PERIODOGRAM METHOD FOR MA(L)

The MA1 method [16], [25] calculates a temporal periodogram mean $J_{f_{MA}}$ defined as $J_{f_{MA}} = J_f|_{f_n=f_{MA,n}}$, where

$$J_f[k] := E\left\{\frac{1}{N}\left|\sum_{n=0}^{N-1}(f_n[\boldsymbol{u}]-\mu)\,\mathcal{W}_N^{nk}\right|^2\right\}, \tag{7}$$

for $k = 0, \ldots, N-1$. The temporal periodogram mean $J_{f_{MA}}$ is an asymptotically unbiased estimate of the temporal PSD of f_{MA} as N increases. We can then obtain $J_{f_{MA}}[k] = |H_k|^2\, J_g[k]$, where H_k is the discrete Fourier transform of h_ℓ and J_g is the temporal periodogram mean of g in a similar manner to (7) [32]. From the independence assumption on g_n along n, J_g is constant. Because $H_0 = 1$, we obtain $J_{f_{MA}}[k] = |H_k|^2 J_{f_{MA}}[0]$, where $J_{f_{MA}}[0]$ is an estimate of the PSD of f_{MA} at zero frequency [45], [46]. Therefore, from Parseval's theorem, the LCF of (3) satisfies $r_{MA} = N^{-1}\sum_{k=0}^{N-1}|H_k|^2$; thus, the LCF from MA1 can be expressed as [25]

$$r_{MA} = \frac{\frac{1}{N}\sum_{k=0}^{N-1} J_{f_{MA}}[k]}{J_{f_{MA}}[0]}. \tag{8}$$

Kim [47] suggested high-precision measurement methods that can be used to estimate $J_{f_{MA}}$. In (8), $J_{f_{MA}}[0]$ is the temporal periodogram mean at zero frequency and is important for calculating accurate LCF values because $J_{f_{MA}}[0]$ is the denominator of the LCF in (8). Menser *et al.* [48] interpolated $J_{f_{MA}}[0]$ from neighbor values. Kim [46], and Gonzales-Lopez and Canpos-Morcillo [49] employed efficient detrending schemes to obtain accurate zero-frequency PSD values. Ji *et al.* [50] calculated a trend variance to alleviate the influence of unpredictable trends. Kim and Lee [45] proposed a high-precision estimate for the zero-frequency PSD.

B. MA2: TEMPORAL CORRELATION METHOD FOR MA(L)

The MA2 method [26] uses temporal correlation coefficients between the same position pixels acquired at different times. For appropriately measured correlations, MA2 can be insensitive to various disturbances compared to MA1. Let ρ_ℓ denote the Pearson correlation coefficient of $f_{MA,n}$ and be defined as $\rho_\ell := \mathrm{Cov}\{f_{MA,0}[\boldsymbol{u}], f_{MA,\ell}[\boldsymbol{u}]\}/\mathrm{Var}\{f_{MA,0}[\boldsymbol{u}]\}$, for pixel positions $\boldsymbol{u}$ and $\ell = 0, \ldots, L$. Kim and Lee [26] showed that the LCF of (3) can be a function of ρ_ℓ as

$$r_{MA} = \frac{1}{2\sum_{\ell=0}^{L}\rho_\ell - 1}. \tag{9}$$

Here, if $\rho_\ell = a^\ell$, then $\lim_{L\to\infty} r_{MA}\big|_{\rho_\ell=a^\ell} = r_{AR}$ holds [51]. Furthermore, for $L = 1$ and a relatively small a, $1/(2a+1) \approx (1-a)/(1+a)$. Hence, we can obtain an approximation of $r_{MA} \approx r_{AR}$ holds, where $\rho_0 = 1$ and $\rho_1 = a$. In a similar discussion of (6), a parameter a can be sufficient to calculate LCF even for the MA(L) model if a is relatively small.

C. MA3, MA4: LINE ESTIMATE METHODS FOR MA(L)

For the continuous X-ray source, Kim and Lee [27] proposed line estimation methods, which are referred to as MA3 and MA4. Note that the IEC62220 standards recommend using a continuous X-ray source to control the X-ray quality. We assume that the X-ray tube turns off after reading the gate line of $u_1 = u^o$, for $u_2 = 0, \ldots, U-1$, while the frame for $n = 0$ is scanning. Let $\bar{g}_n$ denote a lag-free image sequence for the nth frame. For the frame of $n = 0$, the pixel $\bar{g}_0$ of the gate line of u_1 satisfies

$$E\{\bar{g}_0[\boldsymbol{u}]\} = \mu + \left(u^o - u_1\right)\nu\phi_{u_1-u^o-1}, \tag{10}$$

for $u_2 = 0, \ldots, U-1$. We can observe from (10) that $E\{\bar{g}_0[\boldsymbol{u}]\}$ linearly decreases after $u_1 = u^o$. Here, ϕ_ℓ is a unit step function defined as $\phi_\ell := 1$, for $\ell \geq 0$ and 0, otherwise. For the frame of $n = 1$, the image satisfies

$$E\{\bar{g}_1[\boldsymbol{u}]\} = \left(u^o - u_1\right)\nu\phi_{u^o-u_1}, \tag{11}$$

for $u_2 = 0, \ldots, U-1$. For $n \geq 2$, $E\{\bar{g}_n[\boldsymbol{u}]\} = 0$ holds. Based on the MA(L) model, let $\bar{f}_{MA,n}$ denote the temporally decaying image frames acquired from the continuous X-ray source and be defined as $\bar{f}_{MA,n}[\boldsymbol{u}] := \sum_{\ell=0}^{L}\bar{g}_{n-\ell}[\boldsymbol{u}]h_\ell$. Kim and Lee [27] proposed an algorithm to measure the LCF based on a summation of squares of line-mean differences using $\bar{f}_{MA,n}$. Light photons exposed into the TFT elements can produce leak currents even when the gate is off [27] as addressed in Appendix A. Crosstalk artifacts can be observed from exposure leaks. For the LCF obtained based on the line

mean difference, the exposure leak signal can distort the measurement of LCF. In order to compensate for the leak signal, the mean of the exposure leak signal is subtracted. We call this method MA3 [27]. Instead of the the line mean difference, we can use a summation of squares of line-mean ratios. This algorithm, which is called MA4, does not require any leak compensation schemes. However, due to the empirical line mean in the denominator, the estimate precision of MA4 can be worse than that of MA3 especially at relatively low doses [27].

D. MA5: GRANFORS-AUFRICHTIG METHOD FOR MA(L)

The MA5 method [24] uses block means of image frames for the pulsed X-ray source. Let $\hat{f}_{MA,n}$ denote the acquired image frames as $\hat{f}_{MA,n}[\boldsymbol{u}] := \sum_{l=0}^{L} \hat{g}_{n-l}[\boldsymbol{u}]h_l$ based on the MA(L) model. Here, $\hat{g}_n$ is defined as $\hat{g}_n[\boldsymbol{u}] := g_n[\boldsymbol{u}]$ for $n \leq 0$, and 0 otherwise. From the LCF for the MA(L) model of (3), the LCF is given as

$$r_{MA} = \frac{1}{\mu^2} \sum_{\ell=0}^{L} \left(E\left\{\hat{f}_{MA,\ell}[\boldsymbol{u}]\right\} - E\left\{\hat{f}_{MA,\ell+1}[\boldsymbol{u}]\right\} \right)^2. \quad (12)$$

E. AR2, AR5: MATSUNAGA METHODS FOR AR(1)

The Matsunaga methods [23], which is referred to as AR2 and AR5, is based on the AR(1) model, where a single parameter a is sufficient to calculate the LCF of r_{AR} from (5).

MA2 uses the L correlation coefficients of ρ_ℓ based on MA(L). In contrast, for the AR(1) model, the first correlation coefficient is sufficient to obtain a parameter for the LCF calculation from (5) as

$$a = \frac{\mathrm{Cov}\left\{f_{AR,0}, f_{AR,1}\right\}}{\mathrm{Var}\left\{f_{AR,0}\right\}}. \quad (13)$$

We term this method, which calculates the LCF using a in (13), AR2. Note that correlation methods for MA(L) and AR(1) are MA2 and AR2, respectively.

For the AR(1) model, let $\hat{f}_{AR,n}$ denote the transient decaying image frames. $\hat{f}_{AR,n}$ is then defined as $\hat{f}_{AR,n}[\boldsymbol{u}] = a\hat{f}_{AR,n-1}[\boldsymbol{u}]+(1-a)\hat{g}_n[\boldsymbol{u}]$ and is acquired for the pulsed X-ray source. The LCF r_{AR} can then be calculated using (5). Using block means from $f_{AR,n}$, parameter a can also be obtained as

$$a = \frac{E\left\{\hat{f}_{AR,1}\right\}}{E\left\{\hat{f}_{AR,0}\right\}}. \quad (14)$$

We term this method AR5. In (14), the frame $\hat{f}_{MA,0}$ is obtained when the X-ray is fully exposed to a pulsed X-ray source and $\hat{f}_{MA,1}$ is obtained when the X-ray turns off.

Generally, the parameter obtained using (14) is used to indicate the detector lag performance for the first frame in percent. However, the method for obtaining the parameter a using (14) can be applied for the pulsed X-ray source. In measuring the block means of (14), the exposure leak signal is not produced because the readout process does not run during the X-ray exposure from the pulsed X-ray source.

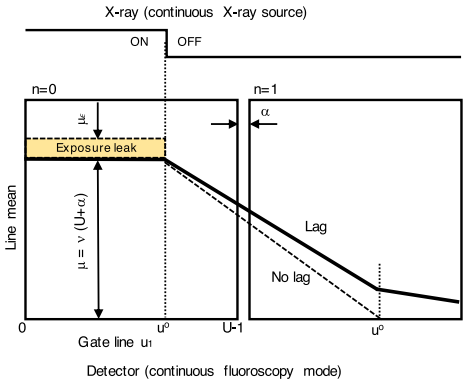

FIGURE 2. Decaying line means from two transient image frames when the X-ray tube turns off at $u = u^o$ of $n = 0$ in an FP dynamic detector. When the X-ray is exposed to the TFT elements the exposure leak signal yields a mean of μ_ϵ (Appendix A).

IV. SIMPLE METHODS BASED ON THE AUTO-REGRESSIVE MODEL

In this section, we propose three LCF measurement methods based on the AR(1) model in order to reduce computational complexities. The basic characteristics of the proposed methods are classified in the place marked "Proposed" in Table 1.

A. AR1: TEMPORAL PERIODOGRAM METHOD FOR AR(1)

We propose an LCF measurement method based on a temporal periodogram under the AR(1) model. We calculate the temporal periodogram mean for the AR(1) model in a similar manner to $J_{f_{MA}}$. Let $J_{f_{AR}}$ denote the temporal periodogram mean of the AR(1) signal $f_{AR,n}$ of (4). From Appendix B, we can obtain

$$r_{AR} = \frac{J_{f_{AR}}[1]}{J_{f_{AR}}[0]}. \quad (15)$$

In (15), $J_{f_{AR}}[0]$ and $J_{f_{AR}}[1]$ are the periodogram values of consequent two images $f_{AR,0}$ and $f_{AR,1}$ for $N = 2$ in (7). Hence, by calculating only these two values, we can simply measure the LCF value from (15) based on the AR(1) model. Note that MA1 requires images as many as $N = 64 - 128$ to calculate LCF from (8). We call this method AR1, which is summarized as follows.

AR1 Method (Temporal Periodogram):

1) Calculate the temporal periodogram means $J_{f_{AR,n}}[0]$ and $J_{f_{AR,n}}[1]$ using (7).
2) Determine r_{AR} based on AR(1) using (15).

Note that the LCF value of the existing MA1 in (8) cannot be equal to that of AR1 in (15) for any N. This fact implies that the proposed AR1 is not a special case of the existing MA1.

B. AR3: DIFFERENCE OF THE LINE MEANS FOR AR(1)

Using the line means, we propose a measurement method based on the AR(1) model in a similar manner to MA3. We consider a transient decaying AR(1) model $\bar{f}_{AR,n}$ for the

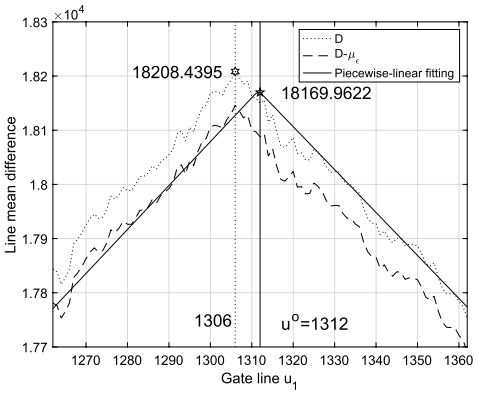

FIGURE 3. Example of the proposed AR3 method based on the line means for the AR(1) model. The measured LCF values are 0.9414 and 0.9385 without μ_ϵ subtraction.

continuous X-ray source as

$$\bar{f}_{AR,n}[\boldsymbol{u}] = a\bar{f}_{AR,n-1}[\boldsymbol{u}] + (1-a)\bar{g}_n[\boldsymbol{u}], \tag{16}$$

where the mean of $\bar{g}_n$ is defined in (10) and (11). For the image frames of $n = 0$ and 1, the line means with respect to the horizontal gate scan u_1 are given as $E\{\bar{f}_{AR,0}[(u_1, u_2)]\} + \mu_\epsilon\phi_{u^o-u_1}$ and $E\{\bar{f}_{AR,1}[(u_1, u_2)]\}$, respectively. as illustrated in Fig. 2. Here, the frame of $n = 0$ contains the leak signal $\mu_\epsilon\phi_{u^o-u_1}$ (Appendix A). Without lag signals, the line mean becomes zero after u^o of $n = 1$ as the dotted line in Fig. 2. However, due to the lag signals, the line mean does not reach zero immediately.

Using the two line means of Fig. 2, let D denote the line mean difference defined as

$$D(u_1) := E\left\{\bar{f}_{AR,0}[(u_1, u_2)]\right\} + \mu_\epsilon\phi_{u^o-u_1} - E\left\{\bar{f}_{AR,1}[(u_1, u_2)]\right\}, \tag{17}$$

for $u_1 = 0, \ldots, U-1$. Note that the line means are independent of u_2. From Appendix C, D of (17) can be rewritten as

$$D(u_1) = \begin{cases} (1-a)\,[\mu + (u_1 - u^o)v] + \mu_\epsilon, \\ \quad \text{for } u_1 = 0, \ldots, u^o - 1, \\ (1-a)\,[\mu + (1-a)(u^o - u_1)v]\,, \\ \quad \text{for } u_1 = u^o, \ldots, U-1. \end{cases} \tag{18}$$

An example of D is illustrated as "D" in Fig. 3, where D can be described with two linear polynomials. The intersection of the left polynomial, which is subtracted by μ_ϵ, and the right polynomial occurs at $u_1 = u^o$. Therefore, a can be given as

$$a = 1 - \frac{D(u^o)}{\mu} \tag{19}$$

and r_{AR} can be calculated using (5). Here, subtracting the exposure leak mean μ_ϵ from the left polynomial implies a leak compensation. We call the LCF measurement from (19) AR3 and summarize the method as follows.

AR3 Method (Line Mean Difference):

0) For a signal mean μ, obtain the leak mean μ_ϵ (Appendix A).
1) Calculate the line means and obtain the difference D of (17).
2) Conduct linear fitting to obtain linear polynomials.
3) Determine u^o from the intersection of the left polynomial with μ_ϵ subtraction and the right polynomial, and obtain a from (19). r_{AR} can then be obtained using (5).

Note that the proposed AR3 uses a line-mean difference of two images instead of complicated summations of squares of line-mean differences of the MA3 case. Hence, the computational complexity of AR3 is much lower than the MA3 case.

In the example of Fig. 3, by subtracting the leak mean μ_ϵ from the left polynomial, the intersection is $u^o = 1,312$ and the LCF is 0.9414. However, without considering the leak mean, the intersection is 1, 306 and the LCF slightly decreases to 0.9385. Hence, in AR3, the LCF value, which is obtained without the leak compensation, is less than the true LCF value.

C. AR4: RATIO OF THE LINE MEANS FOR AR(1)

Similar to MA4, the line mean of $n = 1$ can be divided by the line mean of $n = 0$ to obtain the LCF for the AR(1) model. Let R denote the line mean ratio and be defined as

$$R(u_1) := \frac{E\{\bar{f}_{AR,1}[(u_1,u_2)]\}}{E\{\bar{f}_{AR,0}[(u_1,u_2)]\} + \mu_\epsilon \cdot \phi_{u^o-u_1}}, \tag{20}$$

for $u_1 = 0, \ldots, U-1$. From Appendix C, (20) can be rewritten as

$$R(u_1) = \begin{cases} [a\mu + (1-a)(u^o - u_1)v]/(\mu + \mu_\epsilon), \\ \quad \text{for } u_1 = 0, \ldots, u^o. \\ a, \quad \text{for } u_1 = u^o + 1, \ldots, U-1. \end{cases} \tag{21}$$

An LCF measurement method, which is called AR4, can be summarized as follows.

AR4 Method (Line Mean Ratio):

1) Calculate the line means and obtain the ratio R of (20).
2) Conduct a linear fitting for R to obtain a. r_{AR} can then be calculated using (5).

An example of the proposed AR4 method is illustrated in Fig. 4. The intersection between the linear polynomials occurs at 1, 311, which is close to $u^o = 1,312$ of AR3 as shown in Fig. 3. Hence, we can approximetely obtain the X-ray off position u^o from the intersection in AR4. Note that AR4 does not require the leak compensation in a similar manner to MA4 and has a lower encoding complexity than the MA4 case. However, as mentioned in Subsection III-C, empirical estimates of the denominator of (20) can worse the LCF estimate precision especially at low doses compared to the AR3 case.

V. RESULTS AND DISCUSSIONS

In this section, we first introduce the experimental results of the LCF measurements for an FP detector. A dynamic detector of DRTECH Co. Ltd. (www.drtech.co.kr) was used, where the a-IGZO TFT panel with a-CsI(TI) scintillator controlled the photodiodes. X-ray raw image frames were acquired under the continuous fluoroscopy mode at frame rates of

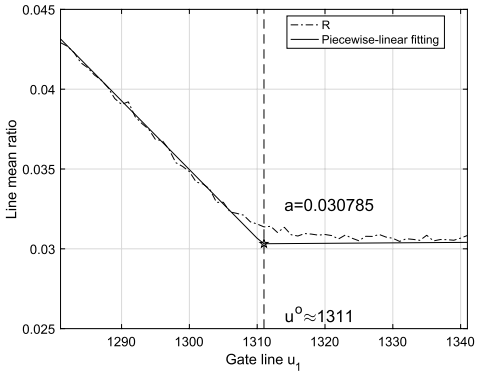

FIGURE 4. Example of the proposed AR4 method based on the line means for the AR(1) model. The measured LCF value is 0.9403.

10 fps and 30 fps under the RQA5 condition of IEC62220-1-3 for the continuous X-ray source. We next discuss several issues on measuring LCF values.

A. EXPERIMENTAL RESULTS

With respect to different incident doses, Figs. 5 and 6 show the LCF values measured using the eight measurement methods of MA1-MA4 and AR1-AR4 including the proposed AR1, AR3, and AR4. In this experiment, we did not consider MA5 and AR5, which require the pulsed X-ray source. The mean values of the measured LCF values over the doses are summarized in Table 2, where the LCF values are similar to the values introduced in the literature [23]–[27], [52]. For 10 fps, the mean LCF values for the MA(L) and AR(1) models were $r = 0.9364$ and $r = 0.9398$, respectively. The methods MA3, MA4, AR3, and AR4, which are based on line means, provided consistent LCF values for a wide range of doses and decreasing values at low doses as shown in Fig. 6. MA2 and AR2, which are based on variances, provided constant LCF values for all doses. However, MA1 and AR1, which are based on temporal periodogram means, do not show consistent values over the doses.

B. NONUNIFORM TEMPORAL GAIN CORRECTION

In calculating J_f of (7) for MA1 and AR1, various disturbances, such as NTG, can distort LCF measuring. To describe NTG, we introduce a weakly stationary random sequence γ_n with mean $E\{\gamma_n\} = 1$ and variance $\mathrm{Var}\{\gamma_n\}$, and modify the image model of (2) considering NTG as [26], [33]

$$q_n[\boldsymbol{u}] := \gamma_n f_n[\boldsymbol{u}], \tag{22}$$

where q_n is a signal with NTG, and γ_n is independent of the pixel values f_n. In the NTG model of (22), we assume that the variance of γ_n is significantly smaller than the mean of γ_n, i.e., $1 \gg \mathrm{Var}\{\gamma_n\}$. Hence, we can obtain an approximation of $1 + \mathrm{Var}\{\gamma_n\} \approx 1$. Under the assumption of $1 \gg \mathrm{Var}\{\gamma_n\}$ [17], from (7) and Appendix D, we can obtain an approximation of the temporal periodogram mean of q_n as

$$J_q[k] \approx J_f[k] + \mu^2 J_\gamma[k], \tag{23}$$

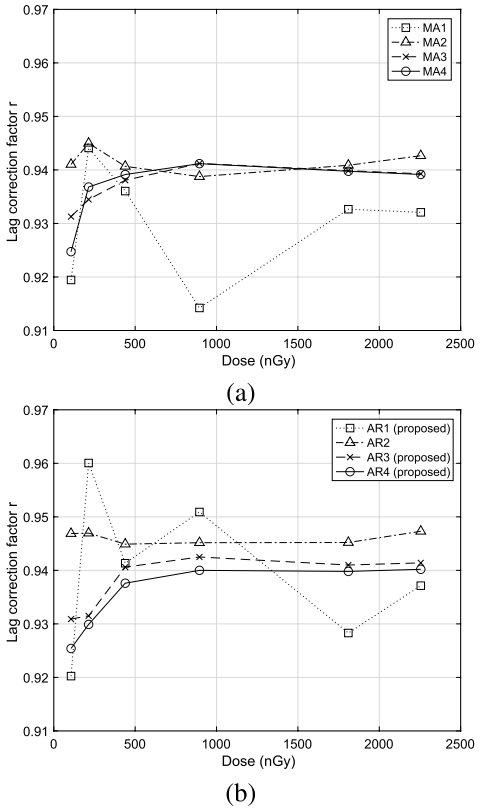

FIGURE 5. Comparisons of the LCF measurements for 10 fps. (a) Comparison of MA1-MA4 for the MA(L) model. (b) Comparison of AR1-AR4 for the AR(1) model.

where J_q and J_γ are defined in a similar manner to J_f using (7). In (23), J_q has a bias of $\mu^2 J_\gamma$, which is due to the NTG of γ_n and is proportional to the square of the signal mean μ. Although J_γ is relatively small, because the signal mean μ is practically large, the bias $\mu^2 J_\gamma$ cannot be negligible. Hence, the bias prevents accurate measurement of J_f from the acquired X-ray images q_n. Low frequencies of k, $J_\gamma[k]$ in particular can indicate large values; thus, the resultant LCF value can be significantly lower than the true LCF [26].

To reduce the bias from NTG [26], [27] for a given n, we can estimate the gain γ_n from a conditional mean $E\{\gamma_n f_n[\boldsymbol{u}] \mid \gamma_n\} = \gamma_n \mu$ and, by dividing the nth frame by the gain γ_n, we can directly correct the NTG of γ_n [25]. Instead of this direct NTG correction, which is a division of γ_n, we can use the notion of image differences as described by Kim [17], and Kim and Lee [51]. Note that this signal-difference approach can alleviate both nonuniform gains and offsets [53].

For an image q with $U \times U$ pixels, the image difference Δq between the upper and lower pixels can be calculated as

$$\Delta q[\boldsymbol{u}] := \frac{1}{\sqrt{2}}\left[q[\boldsymbol{u}] - q\left[\boldsymbol{u} + \left(0, \frac{U}{2}\right)\right]\right], \tag{24}$$

for $\boldsymbol{u} \in \{0, \cdots, U-1\} \times \{0, \cdots, U/2 - 1\}$. The image difference Δq_n, which is defined as $\Delta q_n := \Delta q|_{q=q_n}$, has a mean of zero because the mean of the upper image part is

TABLE 2. Mean values of the measured LCF values of Figs. 5 and 6 over the doses.

fps	MA1	MA2	MA3	MA4	AR1	AR2	AR3	AR4
10	0.9298	0.9415	0.9374	0.9368	0.9397	0.9461	0.9380	0.9355
30	0.9385	0.9431	0.9153	0.9284	0.9437	0.9476	0.9199	0.9345

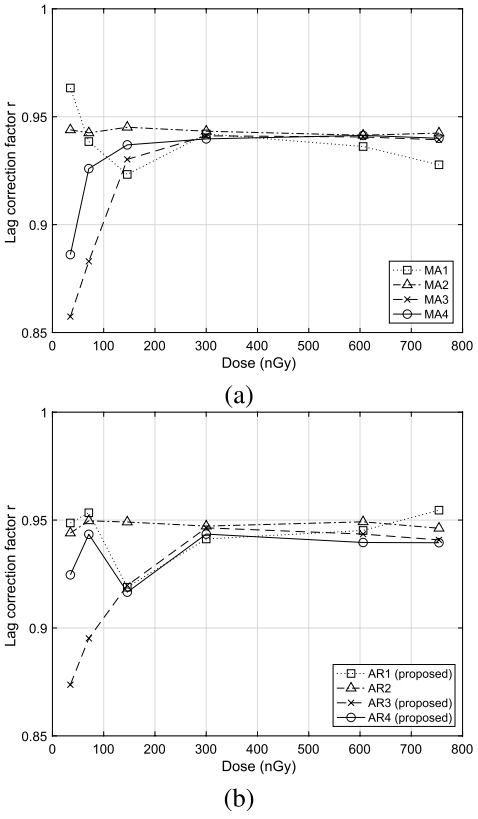

FIGURE 6. Comparisons of the LCF measurements for 30 fps. (a) Comparison of MA1-MA4 for the MA(L) model. (b) Comparison of AR1-AR4 for the AR(1) model.

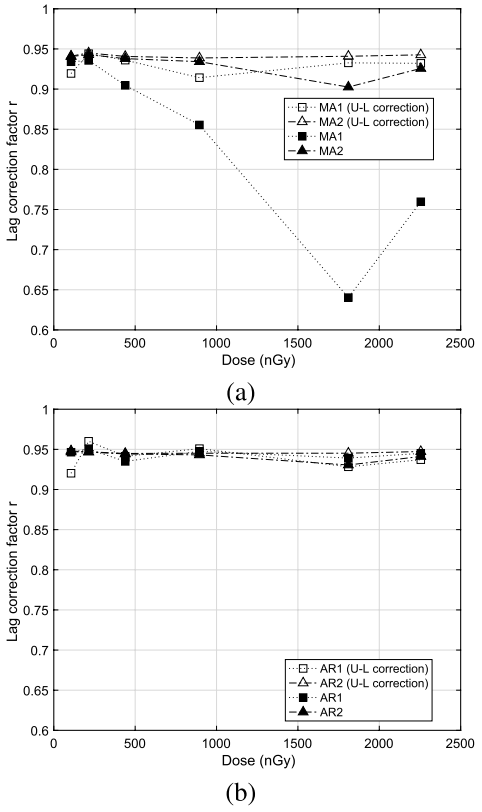

FIGURE 7. Comparisons of the NTG correction using the U-L scheme. (a) Comparison of MA1 and MA2 for the MA(L) model. (b) Comparison of AR1 and AR2 for the AR(1) model.

equal to that of the lower image part within an image frame. In other words, the signal mean of μ in (23) becomes zero; hence, the temporal periodogram mean $J_{\Delta q}$ can approximate the temporal periodogram mean J_f of (7). Therefore, we can obtain an accurate LCF based on the image difference of (24) independent of NTG γ_n. Here, we assume that pixels that are separated by $U/2$ pixels are mutually independent as the α-mixing (or m-dependent) condition [28, p. 387]. We call this preprocessing approach of (24) the U-L scheme.

In calculating the correlations for MA2 and AR2, the NTG of (22) can also distort correlation measuring. Using the acquired image q_n, the measured correlation coefficient is given as $\mathrm{Cov}\{q_0, q_\ell\}/\mathrm{Var}\{q\}$. Here, from the law of total covariance,

$$\mathrm{Cov}\{q_0, q_\ell\} = (1 + \mathrm{Cov}\{\gamma_0, \gamma_\ell\})\mathrm{Cov}\{f_0, f_\ell\} + \mu^2\mathrm{Cov}\{\gamma_0, \gamma_\ell\} \quad (25)$$

holds with a bias of $\mathrm{Cov}\{\gamma_0, \gamma_\ell\}(\mathrm{Cov}\{f_0, f_\ell\} + \mu^2)$. Hence, we cannot accurately measure the LCF of (9) by using the correlation coefficients obtained using q_n. Under the assumption of $1 \gg \mathrm{Var}\{\gamma_n\}$, the bias term in (25) can be approximated as $\mu^2\mathrm{Cov}\{\gamma_0, \gamma_\ell\}$. Here, the U-L scheme can be used to eliminate the μ^2 value and thus the bias $\mu^2\mathrm{Cov}\{\gamma_0, \gamma_\ell\}$. The measured correlation coefficient is then expressed as $\mathrm{Cov}\{\Delta q_0, \Delta q_\ell\}/\mathrm{Var}\{\Delta q_0\}$ using the difference Δq_n of (24). Here, $\mathrm{Cov}\{\Delta q_0, \Delta q_\ell\} = \mathrm{Cov}\{f_0, f_\ell\}$ and $\mathrm{Var}\{\Delta q_0\} \approx \mathrm{Var}\{f_0\}$ hold. Therefore, by using the U-L scheme, the LCF value can be accurately estimated from MA2 or AR2. In calculating the covariances, their offsets should be removed [26], [33]. Using conditional covariances in estimating the correlations, we can also efficiently alleviate the NTG problem without any preprocessing [33].

The comparison results for the NTG correction are illustrated in Fig. 7. If we did not apply any gain correction schemes, such as "MA1" and "MA2" in Fig. 7(a), the estimate accuracies were low with respect to the dose because the lowest LCF value, $r = 0.6403$, was significantly lower than the mean LCF values summarized in Table 2. Applying the U-L scheme to alleviate the NTG problem yielded relatively acceptable estimate accuracies as "MA1 (U-L correction)" and "MA2 (U-L correction)" in Fig. 7(a). The estimates of the LCF using the AR1 and AR2 methods are illustrated in

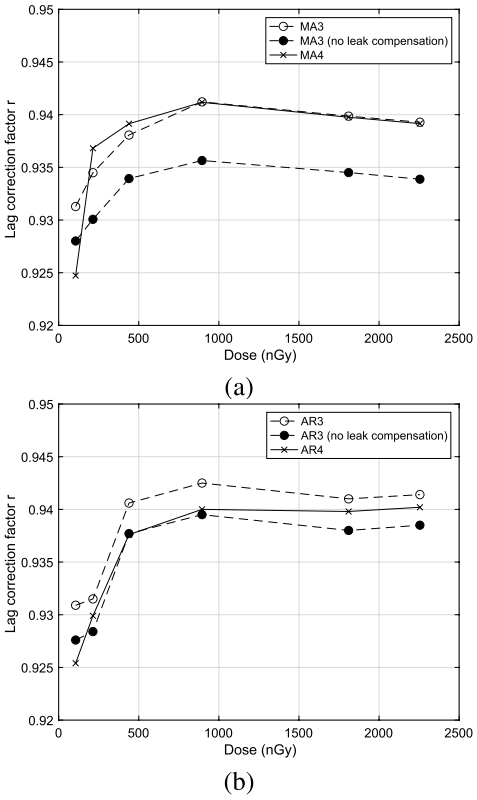

FIGURE 8. Comparisons of the leak compensations. (a) Comparison of MA3 and MA4 for the MA(*L*) model. (b) Comparison of AR3 and AR4 for the AR(1) model.

Fig. 7(b). For AR1 and AR2, it seems that the LCF estimates were less sensitive to NTG because conducting the NTG correction by applying the U-L scheme does not yield evidently different LCF values. Hence, we can obtain reliable LCF values using the AR1 and AR2 methods without carefully considering various disturbances compared to the cases of MA1 and MA2. As Fig. 7(a) shows, the MA1 method without the U-L scheme yielded lower LCF values compared to the other cases.

C. LEAK COMPENSATION

In the MA3 method, applying the leak compensation to correct the exposure leak can remove the increased signal mean and thus provide accurate LCF values. The comparison results for the leak compensation are illustrated in Fig. 8.

We first observe an effect on the leak compensation for the MA3 method from Fig. 8(a). MA3 uses line estimates, which are compensated for the exposure leak and then normalized using a signal mean square. If we did not apply the leak compensation, which is the subtraction of μ_ϵ, for the MA3 method as "MA3 (no leak compensation)" in Fig. 8(a), the estimate curve has a considerable deviation from the leak compensation case of "MA3" in Fig. 8(a). Hence, MA3 should consider the leak compensation using the exposure leak mean to obtain accurate LCF values. On the other hand, MA4 uses a non-uniformly normalized line estimate, where any information on the exposure leak is not required.

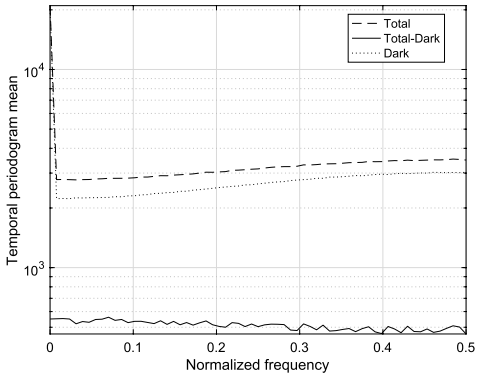

FIGURE 9. Example of the temporal periodogram mean at a low incident dose of 35nGy with 30 fps.

Experimental results on MA4 are compared with those of MA3 as "MA4" in Fig. 8(a). We can observe that, for relatively high doses, the results of MA3 and MA4 are very similar. Hence, we can obtain reliable LCF values from the MA4 method without carefully considering leak signals. However, for relatively low doses, MA4 shows some deviations from the LCF values of MA3.

We next observe an effect of the leak compensation for the proposed AR3 and AR4 methods. The estimates of LCF from the AR3 and AR4 methods are shown in Fig. 8(b). The LCF estimates with the leak compensation ("AR3") is definitely higher than that without the compensation ("AR3 (no leak compensation)"). However, it seems that the LCF estimates are less sensitive to leaks because conducting the leak compensation does not indicate evidently different LCF values as much as those in Fig. 8(a). For AR4, it does not seem to follow the trend of AR3. In particular, AR4 exhibits relatively lower LCF values compared to the AR3 case at low doses. However, the LCF estimates of AR4 are greater than those of AR3 without the leak compensation for most doses. Although the proposed AR4 method does not require any leak compensation, the proposed AR3 method can be employed to obtain further accurate LCF values for a wide range of incident doses.

D. LCF MEASURED AT LOW DOSES

We now observe the measured LCF values at low incident doses. At relatively low doses, the measured LCF values exhibit different trends depending on whether the first or second moment is used. The MA1, MA2, AR1, and AR2 methods, which are based on the second moments, yield consistent LCF values with those of other doses (Figs. 5, 6, and 7). However, for relatively low doses as shown in Fig. 9, both the dark and white temporal periodogram mean curves exhibit increasing curves rather than generally constant or decreasing curves. Hence, the estimates from the methods of the second moment can be inaccurate because the increasing spectrum of the dark images can affect the total spectrum. In contrast, MA3, MA4, AR3, and AR4, which are based on the first moments, yield LCF values that hardly change for a wide range of doses, as Granfors [6] and Hunt *et al.* [54]

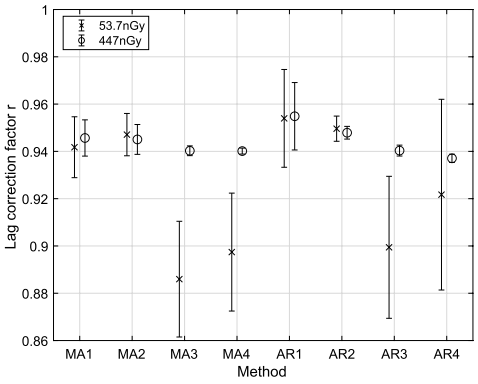

FIGURE 10. Comparison of the estimate precisions for the LCF measurement methods.

mentioned, and they exhibit slightly decreasing values at low doses [27] (Figs. 5, 6, and 8). Starman *et al.* [14] introduced an exposure-dependent lag model, where the mean lag signal increased as the exposure decreased. Busse *et al.* [25] also observed a similar estimate curve from 0.94 to 0.89 as the incident dose decreased.

E. MEASUREMENT PRECISIONS

Fig. 10 shows a comparison of the estimated precisions for the LCF methods by conducting 10 iterations and calculating the empirical mean and standard deviation values. If the standard deviation-to-mean ratio is small, then the estimate precision is high [27].

The methods measured with the steady-state second moments (MA1, MA2, AR1, and AR2) yield better precisions at a low dose of 53.7 nGy than those of the transient first moments (MA3, MA4, AR3, and AR4). However, the methods obtained using the transient first moments yield higher precision for a wide range of incident doses such as 447 nGy than those of the steady-state second moments. We can observe from Fig. 10 that the proposed AR1 method exhibits lower precisions than MA1, where both methods use the temporal periodogram mean. However, because AR1 can use only two frames, i.e., $N = 2$, while $N = 64$ or $N = 128$ for the MA1 method, the proposed AR1 method can significantly reduce the computational complexity. In order to improve the estimate precision of AR1, we can calculate multiple LCF values for multiple pairs of images and conduct their averaging. The proposed AR3 and AR4 methods exhibit high estimate precisions similar to MA3 and MA4 for a wide range of doses. However, the estimate precision of AR3 is better than that of AR4 at relatively low doses as shown in Fig. 10. Note that the proposed methods can provide low computational complexities similar to the AR1 method because of the simple lag model of AR(1).

VI. CONCLUSION

In this paper, we first summarized and analyzed current lag correction factor (LCF) measurement methods considering the two linear lag models: the moving average and autoregressive models. Based on the moving average model, using steady-state image frames, MA1 considers a temporal periodogram mean, and MA2 uses the temporal correlation coefficients. These methods are sensitive to the non-uniform temporal gain (NTG). To alleviate the effects of NTG, we could use the U-L scheme. MA5 uses the block means of the temporally decaying image frames after the X-ray turns off for the pulsed X-ray source. MA3 and MA4 uses line estimation methods to extend MA5 to the continuous X-ray source. Here, MA3 requires an exposure leak compensation. Based on an autoregressive model, AR2 and AR5 use a correlation coefficient and mean ratio, respectively. We next propose three LCF measurement methods as in simplified forms for the autoregressive model based on the notions of the temporal periodogram mean and line means. The proposed methods can simply measure the LCF values by measuring a single parameter for the autoregressive model of order 1 with performances comparable to the methods of the moving average model. Using steady-state image frames, we can use the proposed AR1 method, which is based on the temporal periodogram mean. If decaying image frames after the X-ray tunes off are available, we can use the proposed AR3 or AR4 methods, which can provide high-precision estimates based on line means. Here, AR3 method requires an exposure leak compensation.

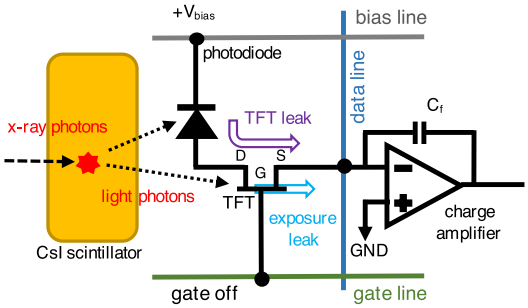

FIGURE 11. Pixel photodiode and a readout circuit with TFT. The TFT and exposure leak signals are produced due to light photons.

APPENDIX A: LEAK SIGNAL MEANS

The readout circuit with TFT is illustrated in Fig. 11. We can consider following types of leak signals concerned with the photosensitive TFT switch.

- TFT leak signal
- Exposure leak signal

The TFT leak signal is formed from a charge leakage of charged photodiodes through TFT when the gate is off and is dependent on the drain-source voltage or the amount of charge that is integrated from the incident light photons at the photodiodes as shown in Fig. 11 [35]. The a-IGZO TFT can increase the mobility and decrease the leak current when the TFT gate is off compared to the amorphous Si case [37], [52], [55], [56]. However, a-IGZO TFT also suffers from permanent or metastable changes in the gate voltage shifts and thus produces TFT leak current due to environment effects including exposure to light [37], [38]. The exposure

leak signal is from the charges produced by TFT elements by the incident light or UV photons to the TFT elements as shown in Fig. 11. Hence, this leak signal is dependent on the incident exposure strength and is independent of the integrated charges of photodiodes. In order to reduce both leak signals, a metallic light shield for the TFT gate can be considered based on an inverted TFT structure [35]. Besides the TFT and exposure leak signals, there are leak currents of amorphous TFT from channel charge emission [39], [57].

For a continuous fluoroscopy mode under an x-ray tube with a constant potential generator [58], a pixel integrates charges during the image frame period of $U + \alpha$ pixels. Hence, for a given pixel, the signal mean μ can be represented as $\mu := \nu \cdot (U + \alpha)$ (DV, digital value), where ν (DV/pixel) is a value yielded for a pixel period and is dependent on the incident exposure [27].

We first consider the TFT leak signal. When scanning pixels for a steady state image sequence, the connected $U - 1$ photodiodes have increasing charges depending on the gate line position u_1. Thus, the accumulated signal value is given as

$$\nu \left[\sum_{k=1}^{U+\alpha-1} k - \sum_{k=1}^{\alpha-1} (k + u_1 + 1) \right], \tag{A 1}$$

for $u_1 = 0, \ldots, U - 1$, and can be expanded as

$$\begin{aligned} &\frac{\nu}{2} \left[(U + \alpha)(U_1 + \alpha - 1) - (2u_1 + \alpha + 1)\alpha \right] \\ &= \frac{\nu}{2} \left[U(U - 1) + 2(U - u_1 - 1)\alpha \right]. \end{aligned} \tag{A 2}$$

Assume that each pixel produces a TFT leak ξ_T (1/pixel) per signal mean. Letting $\mu_T[u_1]$ denote the accumulated TFT leak signal, we can obtain μ_T by multiplying the TFT leak coefficient ξ_T to (A 1) as

$$\mu_T[u_1] := \xi_T \mu \frac{U(U - 1) + 2(U - u_1 - 1)\alpha}{2\,(U + \alpha)}. \tag{A 3}$$

From (A 3), we can observe that the TFT leak signal is strictly decreasing as u_1 increases. Because $\lim_{\alpha \to 0} \mu_T[u_1] = \xi_T \mu \cdot (U - 1)/2$, the TFT leak signal is constant over u_1 if there is no gap between image frames.

We now observe the exposure leak signal. Assume that an exposed TFT element produces an exposure leak of ξ_ϵ per signal mean. The signal mean with the accumulated exposure leak can then be given as

$$\mu_\epsilon := \xi_\epsilon \mu U \tag{A 4}$$

if U horizontal pixels are exposed to light. Hence, the signal mean μ_f, which include both leak signals, can be written as

$$\mu_f[u_1] = \mu + \mu_T[u_1] + \mu_\epsilon. \tag{A 5}$$

We now measure the leak coefficients ξ_T and ξ_ϵ from image frames with Pb plate shadows as in Fig. 12. From the beginning of the second frame, we can observe an added

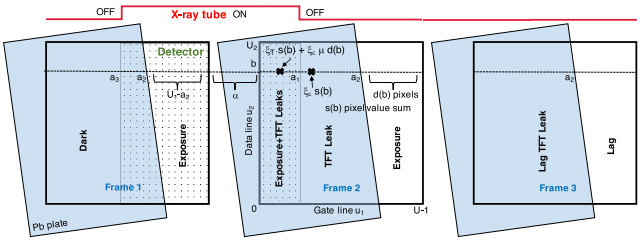

FIGURE 12. Measurements of the leak coefficients from the image frames with Pb plate shadows [27]. The image frames are acquired from a dynamic detector under the continuous fluoroscopy mode for the continuous X-ray.

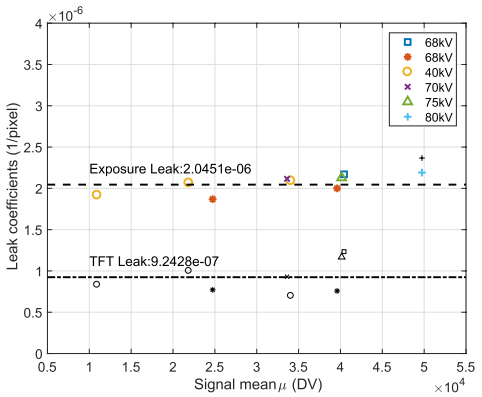

FIGURE 13. Leak coefficients ξ_T and ξ_ϵ with respect to the signal mean μ for various X-ray tube voltages. A CsI(Tl)-scintillator dynamic detector (DRTECH Co. Ltd., www.drtech.co.kr) with 1,644 × 1.652 pixels of a 98 μm/pixel pitch was used. The scan time for a pixel was 104.24 μs with 5 fps and the frame gap was α = 274.65 pixels.

leak signal from both TFT and exposure leak signals as "Exposure+TFT Leaks" and can be expressed as

$$\xi_T s(b) + \xi_\epsilon \mu d(b), \tag{A 6}$$

In (A 6), $\xi_T s(b)$ can be obtained at "TFT Leak" in Fig. 12. Here, $s(b)$ is the accumulated mean values from the pixels, which are connected to the corresponding data line and are charged from the x-ray exposure of the right part, and is given as $s(b) := \sum_{u_1=a_2}^{U-1} p(u_1, b)$ at $u_2 = b$. Hence, we can obtain ξ_T. By subtracting $\xi_T s(b)$ from (A 6), we can obtain $\xi_\epsilon \mu d(b)$. Here, $d(b)$ is the number of exposed pixels that are connected to the corresponding data line and is given as $d(b) := \sum_{u_1=a_2}^{U-1} 1$. Hence, we can obtain ξ_ϵ. Measured leak coefficients are illustrated in Fig. 13.

APPENDIX B: TEMPORAL PERIODOGRAM FOR AR(1)

From (4) and (7), the temporal periodogram of $f_{AR,n}$ can be expanded as

$$\begin{aligned} J_{f_{AR}}[0] &= E\left\{ \frac{1}{2} \left| (f_0 - E\{f_0\}) + (f_1 - E\{f_1\}) \right|^2 \right\} \\ &= \mathrm{Var}\{f_{AR,0}\} + \mathrm{Cov}\{f_{AR,0}, f_{AR,1}\} \end{aligned} \tag{B 1}$$

and

$$\begin{aligned} J_{f_{AR}}[1] &= E\left\{ \frac{1}{2} \left| (f_0 - E\{f_0\}) - (f_1 - E\{f_1\}) \right|^2 \right\} \\ &= \mathrm{Var}\{f_{AR,0}\} - \mathrm{Cov}\{f_{AR,0}, f_{AR,1}\}, \end{aligned} \tag{B 2}$$

for $N = 2$. Hence, from the LCF of AR(1) in (5), we can obtain (15).

APPENDIX C: LINE MEAN DIFFERENCE

The line mean of the frame of $n = 0$ is given as

$$\begin{aligned} &E\{\bar{f}_{AR,0}[\boldsymbol{u}]\} + \mu_\epsilon \phi_{u^o-u_1} \\ &\quad = aE\{\bar{f}_{AR,-1}[\boldsymbol{u}]\} + (1-a)E\{\bar{g}_0[\boldsymbol{u}]\} + \mu_\epsilon \phi_{u^o-u_1} \\ &\quad = \mu + (1-a)(u^o-u_1)\nu\phi_{u_1-u^o-1} + \mu_\epsilon \phi_{u^o-u_1} \quad \text{(C 1)} \end{aligned}$$

based on the AR(1) model of (16). In (C 1), μ_ϵ is the exposure leak mean [27] as shown in Fig. 2. The image frame of $n = 1$ is $\bar{f}_1[\boldsymbol{u}]$, and its line mean is given as

$$\begin{aligned} &E\{\bar{f}_{AR,1}[\boldsymbol{u}]\} \\ &\quad = aE\{\bar{f}_{AR,0}[\boldsymbol{u}]\} + (1-a)E\{\bar{g}_{-1}[\boldsymbol{u}]\} \\ &\quad = aE\{\bar{f}_{AR,0}[\boldsymbol{u}]\} + (1-a)(u^o-u_1)\nu\phi_{u^o-u_1}, \quad \text{(C 2)} \end{aligned}$$

where $E\{\bar{f}_{AR,0}[\boldsymbol{u}]\}$ can be obtained using (C 1). Hence, from (C 1) and (C 2), we can obtain the line mean difference D of (18). Note that the line means can be estimated using the sample means along data line u_2.

APPENDIX D: BIAS FROM THE NONUNIFORM TEMPORAL GAIN

For a weakly stationary sequence f_n, consider a sequence $q_n = \gamma_n f_n[\boldsymbol{u}]$, where γ_n is defined in (22). The temporal periodogram mean of q_n is $J_q[k] = E\{N^{-1}|\sum_{n=0}^{N-1}(\gamma_n f_n[\boldsymbol{u}] - \mu)\mathcal{W}_N^{nk}|^2\}$ and can be expanded as

$$\begin{aligned} J_q[k] &= (1 + \mathrm{Var}\{\gamma_n\})\,\mathrm{Var}\{f_n\} \\ &\quad + \frac{2}{N}\left[\sum_{\ell=1}^{N-1}\sum_{n=0}^{N-\ell-1}\Gamma(n, n+\ell)\cos\left(2\pi\frac{k\ell}{N}\right)\right] \\ &\quad + \mu^2 J_\gamma[k], \end{aligned} \quad \text{(D 1)}$$

where $\Gamma(n, n+\ell) := (1 + \mathrm{Cov}\{\gamma_n, \gamma_{n+\ell}\})\,\mathrm{Cov}\{f_n, f_{n+\ell}\}$. From the assumption that $1 \gg \mathrm{Var}\{\gamma\}$, we can obtain approximations as $(1 + \mathrm{Var}\{\gamma_n\}) \approx 1$ and $\Gamma(n, n+\ell) \approx \mathrm{Cov}\{f_n, f_{n+\ell}\}$. Hence, using (D 1) and the relationship of J_f as

$$\begin{aligned} J_f[k] &= \mathrm{Var}\{f_n\} \\ &\quad + \frac{2}{N}\left[\sum_{\ell=1}^{N-1}\sum_{n=0}^{N-\ell-1}\mathrm{Cov}\{f_n, f_{n+\ell}\}\cos\left(2\pi\frac{k\ell}{N}\right)\right], \end{aligned} \quad \text{(D 2)}$$

we can obtain an approximation of

$$J_q[k] \approx J_f[k] + \mu^2 J_\gamma[k], \quad \text{(D 3)}$$

where a bias term $\mu^2 J_\gamma[k]$ is produced from the NTG γ_n.

REFERENCES

[1] M. J. Yaffe and J. A. Rowlands, "X-ray detectors for digital radiography," *Phys. Med. Biol.*, vol. 42, no. 1, pp. 1–39, Jan. 1997.
[2] K. Hasegawa, K. Mochiki, H. Takahashi, S. Namatame, and Y. Satow, "Imaging system with an amorphous silicon linear sensor," *Rev. Sci. Instrum.*, vol. 60, no. 7, pp. 2284–2286, Jul. 1989.
[3] T. Kamiya, K. Nomura, and H. Hosono, "Present status of amorphous In–Ga–Zn–O thin-film transistors," *Sci. Technol. Adv. Mater.*, vol. 11, no. 4, Feb. 2010, Art. no. 044305.
[4] R. A. Street, *Hydrogenated Amorphous Silicon* (Cambridge Solid State Science Series). Cambridge, U.K.: Cambridge Univ. Press, 1991.
[5] H. Wieczorek, "Effects of trapping in a-Si:H diodes," *Solid State Phenomena*, vols. 44–46, pp. 957–972, Jul. 1995.
[6] P. Granfors, "Performance characteristics of an amorphous silicon flat-panel X-ray imaging detector," *Proc. SPIE*, vol. 3659, pp. 480–490, May 1999.
[7] Z. B. Alfassi, Y. Ifergan, U. Wengrowicz, and M. Weinstein, "On the elimination of the afterglow of CsI(Tl) scintillation detector," *Nucl. Instrum. Methods Phys. Res. A, Accel. Spectrom. Detect. Assoc. Equip.*, vol. 606, no. 3, pp. 585–588, Jul. 2009.
[8] M. Overdick, T. Solf, and H. A. Wischmann, "Temporal artifacts in flat dynamic X-ray detector," *Proc. SPIE*, vol. 4320, pp. 47–58, Jun. 2001.
[9] H. Kawashima, R. Tanaka, K. Ichikawa, K. Matsubara, H. Iida, and S. Sanada, "Investigation of image lag and modulation transfer function in fluoroscopy images obtained with a dynamic flat-panel detector," *Radiolog. Phys. Technol.*, vol. 6, no. 2, pp. 367–374, Jul. 2013.
[10] L. Zhu, N. R. Bennett, and R. Fahrig, "Scatter correction method for X-ray CT using primary modulation: Theory and preliminary results," *IEEE Trans. Med. Imag.*, vol. 25, no. 12, pp. 1573–1587, Dec. 2006.
[11] E. G. Shapiro, R. E. Colbeth, E. T. Daley, I. D. Job, I. P. Mollov, T. I. Mollov, J. M. Pavkovich, P. G. Roos, J. M. Star-Lack, and C. A. Tognina, "Multidetector-row CT with a 64-row amorphous silicon flat panel detector," *Proc. SPIE*, vol. 6510, pp. 1267–1279, Mar. 2007.
[12] J. Baek and N. J. Pelc, "Effect of detector lag on CT noise power spectra," *Med. Phys.*, vol. 38, no. 6Part1, pp. 2995–3005, May 2011.
[13] R. Tanaka, K. Ichikawa, S. Mori, S. Dobashi, M. Kumagai, H. Kawashima, S. Minohara, and S. Sanada, "Investigation on effect of image lag in fluoroscopic images obtained with a dynamic flat-panel detector (FPD) on accuracy of target tracking in radiotherapy," *J. Radiat. Res.*, vol. 51, no. 6, pp. 723–731, 2010.
[14] J. Starman, J. Star-Lack, G. Virshup, E. Shapiro, and R. Fahrig, "A non-linear lag correction algorithm for a-Si flat-panel X-ray detectors," *Med. Phys.*, vol. 39, no. 10, pp. 6035–6047, Sep. 2012.
[15] R. F. Wagner and J. M. Sandrik, "An introduction to digital noise analysis," in *The Physics of Medical Imaging: Recording System Measurements and Techniques*. New York, NY, USA: American Association of Physicist in Medicine, 1979, pp. 524–545.
[16] *Medical Electrical Equipment Characteristics of Digital X-Ray Imaging Devices—Part1-3: Determination of the Detective Quantum Efficiency Detectors Used in Dynamic Imaging*, document IEC 62220-1-3, International Electrotechnical Commission, Geneva, Switzerland, 2007.
[17] D. S. Kim, "Noise power spectrum measurements in digital imaging with gain nonuniformity correction," *IEEE Trans. Image Process.*, vol. 25, no. 8, pp. 3712–3722, Aug. 2016.
[18] R. B. Blackman and J. W. Tukey, *The Measurement of Power Spectra From the Point of View of Communications Engineering*. New York, NY, USA: Dover Publication, 1958.
[19] G. M. Jenkins and D. G. Watts, *Spectral Analysis and its Applications*. San Francisco, CA, USA: Holden-Day, 1969.
[20] A. Papoulis, *Probability, Random Variables, and Stochastic Processes*, 3rd ed. New York, NY, USA: McGraw-Hill, 1991.
[21] B. Porat, *Digital Processing of Random Signals: Theory and Methods*. Upper Saddle River, NJ, USA: Prentice-Hall, 1994.
[22] J. G. Proakis and D. Manolakis, *Digital Signal Processing*, 4th ed. Upper Saddle River, NJ, USA: Prentice-Hall, 2007.
[23] Y. Matsunaga, F. Hatori, H. Tango, and O. Yoshida, "Analysis of signal to noise ratio of photoconductive layered solid-state imaging device," *IEEE Trans. Electron Devices*, vol. 42, no. 1, pp. 38–42, Jan. 1995.
[24] P. R. Granfors and R. Aufrichtig, "DQE(f) of an amorphous-silicon flat-panel X-ray detector: Detector parameter influences and measurement methodology," *Proc. SPIE*, vol. 3977, pp. 2–13, Apr. 2000.
[25] F. Busse, W. Ruetten, H. A. Wischmann, B. Geiger, M. Spahn, R. J. M. Bastiaens, and T. Ducourant, "Methodology to measure fundamental performance parameters of X-ray detectors," *Proc. SPIE*, vol. 4320, pp. 287–298, Jun. 2001.
[26] D. S. Kim and E. Lee, "Signal lag measurements based on temporal correlations," *IEEE Signal Process. Lett.*, vol. 28, pp. 21–25, 2021.
[27] D. S. Kim and E. Lee, "Measurement of the lag correction factor in low-dose fluoroscopic imaging," *IEEE Trans. Med. Imag.*, vol. 40, no. 6, pp. 1661–1672, Jun. 2021.

[28] P. Billingsley, *Probability and Measure, Anniversary Edition*. Hoboken, NJ, USA: Wiley, 2012.
[29] R. J. Wilks, *Principles of Radiological Physics*, 2nd ed. Edinburgh, Scotland: Churchill Livingston, 1987.
[30] J. M. Boone, *Ch. 1 X-Ray Production, Interaction, and Detection in Diagnostic Imaging: Physics and Psychophysics*, vol. 1. Washington, DC, USA: SPIE, 2000.
[31] J. T. Bushberg, J. A. Seibert, J. E. M. Leidholdt, and J. M. Boone, *The Essential Physics of Medical Imaging*, 4th ed. New York, NY, USA: Wolters Kluwer, 2021.
[32] A. V. Oppenheim and R. W. Schafer, *Discrete-Time Signal Processing*, 3rd ed. New York, NY, USA: Prentice-Hall, 2010.
[33] E. Lee and D. S. Kim, "Conditional covariances for the signal lag measurements in fluoroscopic imaging," *Diagnostics*, vol. 12, no. 1, p. 87, Dec. 2021.
[34] D. S. Kim and E. Lee, "Empirical noise power spectrum based on the image subtraction in radiography imaging," in *Proc. IEEE Nucl. Sci. Symp., Med. Imag. Conf. Room-Temp. Semiconductor Detect. Workshop (NSS/MIC/RTSD)*, Oct. 2016, pp. 1–4.
[35] J. A. Rowlands and J. Yorkston, *Ch. 4 Flat Panel Detectors for Digital Radiography, Handbook of Medical Imaging: Physics and Psychophysics*, vol. 1. Washington, DC, USA: SPIE, 2000.
[36] X. Liu, C. C. Shaw, M. C. Altunbas, and T. Wang, "An alternate line erasure and readout (ALER) method for implementing slot-scan imaging technique with a flat-panel detector-initial experiences," *IEEE Trans. Med. Imag.*, vol. 25, no. 4, pp. 496–502, Apr. 2006.
[37] D. H. Chowdhury, P. Migliorate, and J. Jang, "Light induced instability in amorphous indium-gallium-zinc-oxide thin-film transistors," *Appl. Phys. Lett.*, vol. 97, Oct. 2010, Art. no. 173506.
[38] P. Migliorato and J. Jang, *Bias and Light-Induced Instabilities in a-IGZO Thin Film Transistors*. Berlin, Germany: Springer, 2014, pp. 1–27.
[39] J. Smith, A. Couture, and D. Allee, "Charge emission induced transient leakage currents of a-Si:H and IGZO TFTs on flexible plastic substrates," *Electron. Lett.*, vol. 50, no. 2, pp. 105–106, Jan. 2014.
[40] M. S. Bartlett, "Periodogram analysis and continuos spectra," *Biometrika*, vol. 37, nos. 1–2, pp. 1–16, Jun. 1950.
[41] P. D. Welch, "The use of fast Fourier transform for the estimation of power spectra: A method based on time averaging over short, modified periodograms," *IEEE Trans. Audio Electroacoust.*, vol. AU-15, no. 2, pp. 70–73, Jun. 1967.
[42] R. C. Gonzalez and R. E. Woods, *Digital Image Processing*, 3rd. ed. Upper Saddle River, NJ, USA: Prentice-Hall, 2008.
[43] J. C. Dainty and R. Shaw, *Image Science: Principles, Analysis, and Evaluation*. New York, NY, USA: Academic, 1974.
[44] J. Hsieh, O. E. Gurmen, and K. F. King, "Investigation of a solid-state detector for advanced computed tomography," *IEEE Trans. Med. Imag.*, vol. 19, no. 9, pp. 930–940, Sep. 2000.
[45] D. S. Kim and E. Lee, "Estimation of zero-frequency noise power density in digital imaging," *IEEE Signal Process. Lett.*, vol. 25, no. 11, pp. 1755–1759, Nov. 2018.
[46] D. S. Kim, "Measurement of power density at zero frequency with a trend compensation," *IEEE Trans. Signal Process.*, vol. 68, pp. 1964–1973, 2020.
[47] D. S. Kim, "High-precision noise power spectrum measurements in digital radiography imaging," *Med. Phys.*, vol. 45, no. 12, pp. 5461–5471, Dec. 2018.
[48] B. Menser, R. J. M. Bastiaens, A. Nascetti, M. Overdick, and M. Simon, "Linear system models for lag in flat dynamic X-ray detectors," *Proc. SPIE*, vol. 5745, pp. 430–441, Apr. 2005.
[49] A. Gonzalez-Lopez and P.-A. Canpos-Morcillo, "Efficient detrending of uniform images for accurate determination of the noise power spectrum at low frequencies," *Phys. Med. Biol.*, vol. 64, no. 10, pp. 1–11, 2019.
[50] X. Ji, M. Feng, R. Zhang, G. H. Chen, and K. Li, "A experimental method to correct drift-induced error in zero-frequency DQE measurement," *Proc. SPIE*, vol. 10948, Mar. 2019, Art. no. 109480H.
[51] D. S. Kim and E. Lee, "On the performance of the noise power spectrum from the gain-corrected radiography images," *J. Med. Imag.*, vol. 5, no. 1, Mar. 2018, Art. no. 013508.
[52] S. Freestone, R. Weisfield, C. Tognina, I. Job, and R. E. Colbeth, "Analysis of a new indium gallium zinc oxide (IGZO) detector," *Proc. SPIE*, vol. 11312, pp. 970–976, Mar. 2020.
[53] Z. Zhou, F. Gao, H. Zhao, and L. Zhang, "Techniques to improve the accuracy of noise power spectrum measurements in digital X-ray imaging based on background trends removal," *Med. Phys.*, vol. 38, no. 3, pp. 1600–1610, Mar. 2011.
[54] D. C. Hunt, O. Tousignant, and J. A. Rowlands, "Evaluation of the imaging properties of an amorphous selenium-based flat panel detector for digital fluoroscopy," *Med. Phys.*, vol. 31, no. 5, pp. 1166–1175, May 2004.
[55] Y. Li, L. E. Antonuk, Y. El-Mohri, Q. Zhao, H. Du, A. Sawant, and Y. Wang, "Effects of X-ray irradiation on polycrystalline silicon, thin-film transistors," *J. Appl. Phys.*, vol. 99, no. 6, Mar. 2006, Art. no. 064501.
[56] G. Wakimura, Y. Yamauchi, and Y. Kamakura, "Simulation and modeling of off-leakage current in InGaZnO thin-film transistors," *J. Adv. Simul. Sci. Eng.*, vol. 2, no. 1, pp. 201–210, 2015.
[57] F. Lemmi and R. A. Street, "The leakage currents of amorphous silicon thin-film transistors: Channel charge emission," *IEEE Trans. Electron Devices*, vol. 47, no. 12, pp. 2399–2403, Dec. 2000.
[58] R. Aufrichtig, P. Xue, C. W. Thomas, G. C. Gilmore, and D. L. Wilson, "Perceptual comparison of pulsed and continuous fluoroscopy," *Med. Phys.*, vol. 21, no. 2, pp. 245–256, Feb. 1994.

EUNAE LEE (Member, IEEE) received the B.S. and M.S. degrees from the Hankuk University of Foreign Studies, South Korea, in 2014 and 2017, respectively, where she is currently pursuing the Ph.D. degree with the Department of Electronics Engineering. Her research interests include digital signal processing, biomedical image processing, and medical physics.

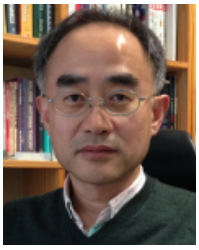

DONG SIK KIM (Senior Member, IEEE) received the B.S., M.S., and Ph.D. degrees in electrical engineering from Seoul National University, Seoul, South Korea, in 1986, 1988, and 1994, respectively. Since 1986, he has been a Research Director with Automan Company Ltd., South Korea, where he has conducted RF circuit design projects. From 1998 to 1999, he was a Visiting Assistant Professor with the School of Electrical and Computer Engineering, Purdue University, West Lafayette, IN, USA. He is with the Hankuk University of Foreign Studies, South Korea, where he is currently a Professor. His research interests include theory of quantization, biomedical image processing, medical physics, sensor networks, and smart grid. He was a Co-recipient of the 2003 International Workshop on Digital Watermarking Best Paper Prize.